

and temperature on the electrical conductivity of wadsleyite and ringwoodite. Owing to the small activation enthalpy, the temperature effect is relatively small: a variation in temperature of ~ 200 K results in a change in conductivity of a factor of ~ 2 . In contrast, the expected water contents in the transition zone range from almost dry ($\sim 10^{-4}$ wt%) to water-saturated (~ 3 wt%), which corresponds to the variation of conductivity by a factor of $\sim 10^3$. Therefore water content is well-constrained by the conductivity data.

The electrical conductivity in the transition zone ranges from $\sim 10^{-2}$ S m $^{-1}$ to ~ 1 S m $^{-1}$ (refs 5–7). This corresponds to water contents of ~ 0.001 to ~ 0.4 wt%. For the upper mantle of the North Pacific Ocean, where a detailed inversion was made using mineral physics constraints⁵, the conductivity in the transition zone is $\sim 10^{-1}$ to $\sim 5 \times 10^{-1}$ S m $^{-1}$ and the corresponding water content in the transition zone is estimated to be ~ 0.1 – 0.2 wt% for the temperature range of 1,825–1,900 K (Fig. 3). The estimated water content in the north Pacific transition zone (~ 0.1 – 0.2 wt%) is significantly higher than the estimated water content in the upper mantle^{8,9} and probably exceeds a critical concentration for partial melting. This suggests that there is a marked layering in water content in the Earth's mantle. This is consistent with a recent model of material circulation⁴ involving the separation of the circulation of incompatible elements from that of major elements near 410 km, but is not consistent with a model involving vertical circulation of hydrogen together with major minerals. However, some regional variation in electrical conductivity was also reported^{5,6}, suggesting a large regional variation in hydrogen content (and temperature) in the transition zone. □

Received 16 September 2004; accepted 31 January 2005; doi:10.1038/nature03426.

1. Smyth, J. R. β -Mg₂SiO₄: A potential host for water in the mantle? *Am. Mineral.* **72**, 1051–1055 (1987).
2. Kawamoto, T., Hervig, R. L. & Holloway, J. R. Experimental evidence for a hydrous transition zone in the early Earth's mantle. *Earth Planet. Sci. Lett.* **142**, 587–592 (1996).
3. Kohlstedt, D. L., Keppler, H. & Rubie, D. C. The solubility of water in α , β and γ phases of (Mg,Fe)₂SiO₄. *Contrib. Mineral. Petrol.* **123**, 345–357 (1996).
4. Bercowski, D. & Karato, S. Whole-mantle convection and the transition-zone water filter. *Nature* **425**, 39–44 (2003).
5. Utada, H., Koyama, T., Shimizu, H. & Chave, A. D. A semi-global reference model for electrical conductivity in the mid-mantle beneath the north Pacific region. *Geophys. Res. Lett.* **30**, 1194–1198 (2003).
6. Ichiki, M. *et al.* Upper mantle conductivity structure of the back-arc region beneath northeastern China. *Geophys. Res. Lett.* **28**, 3773–3776 (2001).
7. Tarits, P., Hautot, S. & Perrier, F. Water in the mantle: Results from electrical conductivity beneath the French Alps. *Geophys. Res. Lett.* **31**, L06612, doi:10.1029/2003GL019277 (2004).
8. Bell, D. R. & Rossman, G. R. Water in Earth's mantle—the role of nominally anhydrous minerals. *Science* **255**, 1391–1397 (1992).
9. Hirth, G. & Kohlstedt, D. L. Water in oceanic upper mantle—implications for rheology, melt extraction and the evolution of lithosphere. *Earth Planet. Sci. Lett.* **144**, 93–108 (1996).
10. Kushiro, I. *et al.* Melting of a peridotite nodule at high pressures and high water pressures. *J. Geophys. Res.* **73**, 6023–6029 (1968).
11. Hirose, K. & Kushiro, I. Partial melting of dry peridotites at high pressures: Determination of compositions of melts segregated from peridotite using aggregates of diamond. *Earth Planet. Sci. Lett.* **114**, 477–489 (1993).
12. Grove, T. L. *et al.* Fractional crystallization and mantle melting controls on calc-alkaline differentiation trends. *Contrib. Mineral. Petrol.* **145**, 515–533 (2003).
13. Karato, S., Paterson, M. S. & Fitz Gerald, J. D. Rheology of synthetic olivine aggregates—implication of grain-size and water. *J. Geophys. Res.* **91**, 8151–8176 (1986).
14. Mei, S. & Kohlstedt, D. L. Influence of water on plastic deformation of olivine aggregates: 1. Diffusion creep regime. *J. Geophys. Res.* **105**, 21457–21469 (2000).
15. Karato, S. & Jung, H. Effects of pressure on high-temperature dislocation creep in olivine. *Phil. Mag.* **83**, 401–414 (2003).
16. Karato, S. The role of hydrogen in the electrical conductivity of the upper mantle. *Nature* **347**, 272–273 (1990).
17. Farver, J. R. & Yund, R. A. Oxygen fugacity in quartz: dependence on temperature and water fugacity. *Chem. Geol.* **90**, 55–70 (1991).
18. Karato, S. in *Inside the Subduction Factory* (ed. Eiler, J.) 138–152 (Am. Geophys. Union, Washington DC, 2003).
19. Paterson, M. S. The determination of hydroxyl by infrared absorption in quartz, silicate glasses and similar materials. *Bull. Mineral.* **105**, 20–29 (1982).
20. Xu, Y., Poe, B. T., Shankland, T. J. & Rubie, D. C. Electrical conductivity of olivine, wadsleyite, and ringwoodite under upper-mantle conditions. *Science* **280**, 1415–1418 (1998).
21. Wood, B. J., Bryndzia, L. T. & Johnson, K. E. Mantle oxidation state and its relationship to tectonic environment and fluid speciation. *Science* **248**, 337–345 (1990).
22. Xu, Y., Shankland, T. J. & Duba, A. G. Pressure effect on electrical conductivity of mantle olivine. *Phys. Earth Planet. Inter.* **118**, 149–161 (2000).

Acknowledgements Z. Jiang and Y. Nishihara provided the technical assistance that made this research possible. This work was supported by the NSF of China and the NSF of the United States.

Authors' contributions S.-I.K. supervised the whole project. The experimental measurements of electrical conductivity were made by X.H. in collaboration with Y.X., and the theoretical interpretation of the results and the geophysical applications were made by S.-I.K. together with Y.X.

Competing interests statement The authors declare that they have no competing financial interests.

Correspondence and requests for materials should be addressed to S.-I.K. (shun-ichiro.karato@yale.edu).

Particle size and energetics of gouge from earthquake rupture zones

Brent Wilson¹, Thomas Dewers¹, Ze'ev Reches¹ & James Brune²

¹School of Geology and Geophysics, University of Oklahoma, Norman, Oklahoma 73019, USA

²Department of Geological Sciences, University of Nevada, Reno, Nevada 89557, USA

Grain size reduction and gouge formation are found to be ubiquitous in brittle faults at all scales^{1–4}, and most slip along mature faults is observed to have been localized within gouge zones^{5,6}. This fine-grain gouge is thought to control earthquake instability^{3,6–8}, and thus understanding its properties is central to an understanding of the earthquake process^{7,9}. Here we show that gouge from the San Andreas fault, California, with ~ 160 km slip, and the rupture zone of a recent earthquake in a South African mine with only ~ 0.4 m slip, display similar characteristics, in that ultrafine grains approach the nanometre scale, gouge surface areas approach $80 \text{ m}^2 \text{ g}^{-1}$, and grain size distribution is non-fractal. These observations challenge the common perception that gouge texture is fractal^{10,11} and that gouge surface energy is a negligible contributor to the earthquake energy budget^{3,9,12}. We propose that the observed fine-grain gouge is not related to quasi-static cumulative slip, but is instead formed by dynamic rock pulverization during the propagation of a single earthquake.

Gouge formation is commonly attributed to wear and attrition of sliding surfaces^{1–3,5,7} or to implosive loading¹³ during earthquakes. Models of wear and attrition¹⁰ predict that progressive shear within gouge zones should lead to grain size reduction due to amplified stresses at grain contacts, and to fractal particle size distributions¹⁰ of the gouge; these predictions are supported by field and experimental observations^{1,2,10,11} with a few exceptions².

However, there are two main pitfalls in standard textural analysis of fine-grained gouge¹⁴. First, optical microscopic analysis and mechanical sieving are restricted to grains a few micrometres in diameter or larger. Second, measurements of the size distribution and surface area of fine-grained materials are susceptible to erroneous results due to the aggregation or agglomeration of extremely fine particles¹⁵. For example, our preliminary measurements of the particle size distribution (PSD) of fault gouge with a laser particle-size analyser reveal profound time drift: the mean grain size of pulverized granite from the San Andreas fault zone (see below) decreased by $26 \pm 13\%$ (s.d.) during 0.5 h of continuous measurement (on the basis of 145 samples¹⁶). This time drift reflects disaggregation into primary grains, as is known for clay mineral aggregates¹⁷. Questions therefore remain open with regard to the size, PSD and surface area of primary particles in fault gouge. To determine these properties accurately we developed a new pro-

cedure of continuous measurements (see Methods). The range of measured particles, down to grains tens of nanometres in size, are also observed directly by scanning electron microscopy.

Pristine gouge is difficult to find. Chemical alteration and lithification alter the texture in exhumed fault zones¹⁸, gouge found at surface rupture zones cannot reflect mechanical conditions at depth, and rupture zones are usually inaccessible at earthquake focal depths. We chose two fault systems that partly remove these limitations. The first is the San Andreas fault, which is a system 1,200 km long that accommodates hundreds of kilometres of right-lateral slip. The better-known exposures of deep parts of the San Andreas fault are inactive segments in southern California that were uplifted from 2–4 km depth^{5,6,18}. Our study focuses on San Andreas gouge exposed in the Tejon Pass region¹⁹ (~100 km north of Los Angeles), alongside the rupture zone of the $M = 8.0$ earthquake in 1857 (Fig. 1a). Here, three sub-parallel fault segments bound a gouge zone 70–100 m wide composed of pervasively pulverized granite¹⁹, distinctly different in PSD and morphology from weathered granites outside the fault zone¹⁹. On the basis of current uplift rates along the San Andreas system²⁰, we estimate that the Tejon Pass region has experienced as much as 4–6 km of uplift since the Pliocene epoch, and that the observed gouge formed at this estimated depth.

South African gold mines, 1.0–3.5 km deep, are shaken daily by thousands of earthquakes. The mines provide access to rupture zones of these earthquakes at focal depth, a unique opportunity for earthquake investigations^{4,21,22}. Gouge is analysed from the rupture zone of the 1997 $M = 3.7$ earthquake in the Hartbeestfontein gold mine (~120 km southwest of Johannesburg, South Africa). This event occurred within unfaulted quartzitic layers at ~2 km depth and produced a new fault (the Bosman fault) later uncovered by mining operations. The Bosman fault zone is at least 5 m wide and 100 m long with 0.37 m of maximum dip-slip displacement, and contains four to six large subparallel segments with hundreds of secondary small fractures (Fig. 1b). Fractures are filled with white gouge that is commonly observed in brittle failure zones of quartzite in mines²³. The gouge of the newborn Bosman fault formed from a single earthquake and was not affected by cumulative slip of multiple seismic events.

The present study includes PSD measurements of ~250 gouge samples from both faults; 155 samples were measured for 0.5 h or more, with eight samples being measured for 45–190 h (see Methods). The results are shown by the following: first, the initial and final PSD (after 72 and 190 h) of the gouge (Fig. 2a); second, the initial and final cumulative frequencies of grain numbers (Fig. 2b); and third, the power-law time decay of mean grain size and the associated increase in surface area of gouge from both faults (Fig. 3). Because the results for the long-duration measurements are generally similar, the figures show only representative samples.

We determined geometric surface area from the PSD of the gouge first by assuming smooth, spherical grains. Independently, the surface areas of six untreated samples of San Andreas gouge were measured with the Barrett–Emmett–Teller (BET) N_2 adsorption technique¹⁵. To estimate grain roughness, we calculated $\lambda = (\text{BET surface area})/(\text{geometric surface area})$; the λ value, 6.6 ± 1.5 , for these samples is similar to a known range of λ of 5.5–22 (ref. 24). With the use of $\lambda = 6.6$, the calculated geometric surface area is converted to equivalent BET surface area (Fig. 3b), revealing surface area values as high as $80 \text{ m}^2 \text{ g}^{-1}$. This surface area is probably a conservative estimate because grain disaggregation does not reach asymptotic values by the end of the long runs (Fig. 3). Scanning electron microscope images of gouge aggregates can also be used to estimate surface area (in $\text{m}^2 \text{ g}^{-1}$) of roughly cubic fragments as $\sim 2/L$, where L is the grain size in micrometres. Thus, fragments of $0.02 \text{ } \mu\text{m}$ of aggregated gouge (Fig. 4) correspond to a surface area of $\sim 100 \text{ m}^2 \text{ g}^{-1}$.

Inspection of Figs 2 and 3 reveals the following three properties.

First, gouge PSD from both faults varies profoundly with run time, changing from an initial range of $0.04\text{--}200 \text{ } \mu\text{m}$ to less than $1 \text{ } \mu\text{m}$ after 72–190 h (Fig. 2a). The mean grain size does not attain asymptotic values (Fig. 3a), indicating that primary grains, which are tens of nanometres in size, might stay aggregated even after long runs. Accordingly, the apparent surface area of gouge grains increases with time and the power-law trend indicates a surface area of $100 \text{ m}^2 \text{ g}^{-1}$ after 300–500 h (Fig. 3b).

Second, gouge samples from the two faults display similar behaviour and final PSD even though the two faults are from strikingly different settings and magnitude.

Third, the grain number–size distribution of disaggregated gouge does not fit a systematic fractal distribution (Fig. 2b) because different slopes (corresponding to different fractal dimensions) are attained with progressive disaggregation. It is therefore inferred that the commonly observed fractal PSD^{1,2,10,11} reflects aggregated gouge grains in a restricted range of coarser grain sizes.

These results permit a better estimation of the earthquake energy balance. The gouge surface area of $\sim 80 \text{ m}^2 \text{ g}^{-1}$ (Fig. 3b) corre-

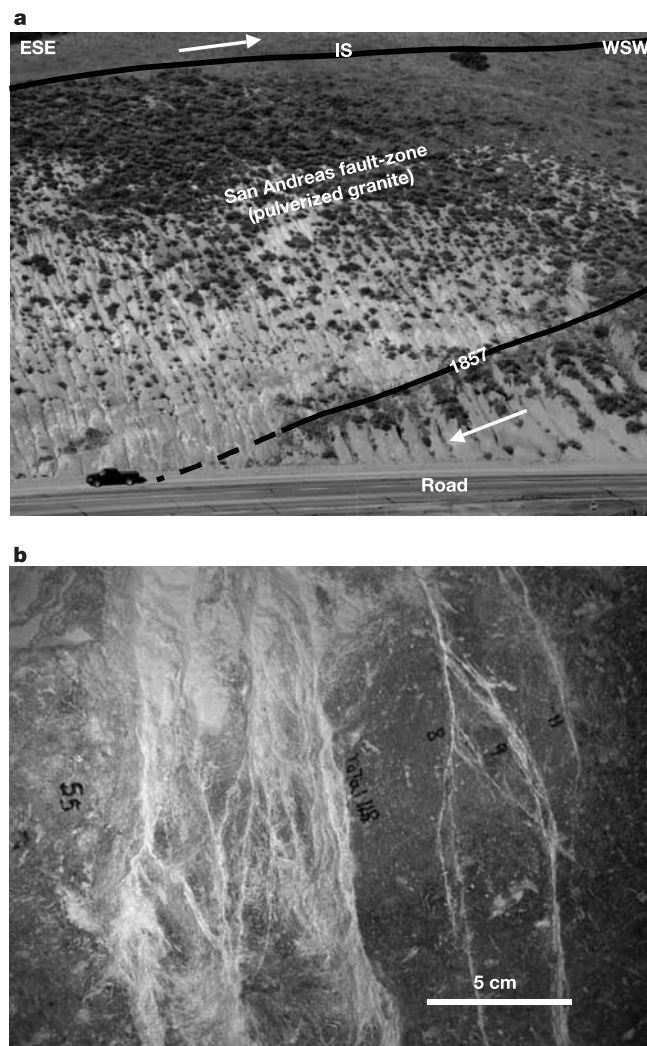


Figure 1 Field setting of the investigated faults. **a**, The San Andreas fault-zone at Tejon Pass, California. The car is shown for scale. IS, inactive fault segment; 1857, slipping segment of the 1857 earthquake. Note the gouge zone 70–100 m wide with badland morphology of the pulverized granite. This exposure and its extensions were mapped, and hundreds of gouge samples were collected. **b**, Close-up view of the fractured zone of the Bosman fault (text). The white striations are coalescing fractures filled with gouge powder (rock flour) that cut across the solid, dark quartzite.

sponds to a surface energy of 0.2–0.36 MJ per m² of the fault surface for a gouge zone 1 mm thick (for a specific surface energy of quartz of 1–1.8 J m⁻²). The Bosman fault earthquake generated tens of subparallel fractures that are each ~1 mm thick and filled with gouge (Fig. 1b); summation of the surface energy, marked here by U_s , of 10–30 fractures yields $U_s \approx 3$ –10 MJ m⁻². This value is roughly equal to the frictional energy calculated for the Bosman earthquake, $U_f = \tau d \approx 8$ –12 MJ m⁻² (τ is the estimated shear stress and d is the measured slip) and it is also similar to the energy release rate of earthquakes of 0.5–5 MJ m⁻² (ref. 25) to 1–100 MJ m⁻² (ref. 26). These energy relations suggest that the surface energy consumed by new gouge that forms during an earthquake can account for 50% or more of earthquake energy.

Finally, we conclude that the observed fine-grained gouge did not form by quasi-static wear and attrition, but rather formed by dynamic rock pulverization during earthquake propagation. This conclusion is based on two outcomes of the analysis. First, the similarity between the PSD of San Andreas gouge with ~160 km of slip at Tejon Pass, and the PSD of the Bosman fault gouge formed by one earthquake with 0.37 m slip, clearly indicates a lack of correlation between slip amount and grain size. Further, because a single earthquake generates the fine-grain gouge, it seems that the governing parameters of gouge formation are earthquake processes and not the cumulative slip attrition. Second, there is an apparent difference between energy consumption by gouge formation during

an earthquake (for example the Bosman fault) and during wear in quasi-static experiments²⁷. In the former, gouge formation consumed ~50% of the earthquake energy (see above), whereas in the latter, gouge formation consumed only 0.2–0.3% of the supplied mechanical energy (we calculate from ref. 27 that $U_f \sim 7$ MJ m⁻² and $U_s \sim 1.5 \times 10^4$ J m⁻², by assuming that their experimental gouge has the same surface area as that in the Bosman fault). An earthquake can pulverize rocks by a few mechanisms: one is the sequence of fault-normal unloading followed by implosive loading during the earthquake passage¹³; another results from the deformation conditions at the tip of the earthquake rupture²⁸. We calculated a maximum tension of ~5 GPa and dilation rates of $\sim 3 \times 10^5$ s⁻¹ at the tip of a mode II fracture propagating at 80% of the shear wave velocity²⁸; these intense conditions are comparable to shock loading²⁹ and could pulverize rocks into gouge.

We now apply the proposed dynamic rock pulverization to the San Andreas fault. If each earthquake in the studied area (Fig. 1a) generated a gouge zone 10 mm thick with ~ 80 m² g⁻¹ (Fig. 3b), the corresponding surface energy would be 2.0–3.6 MJ m⁻² for each

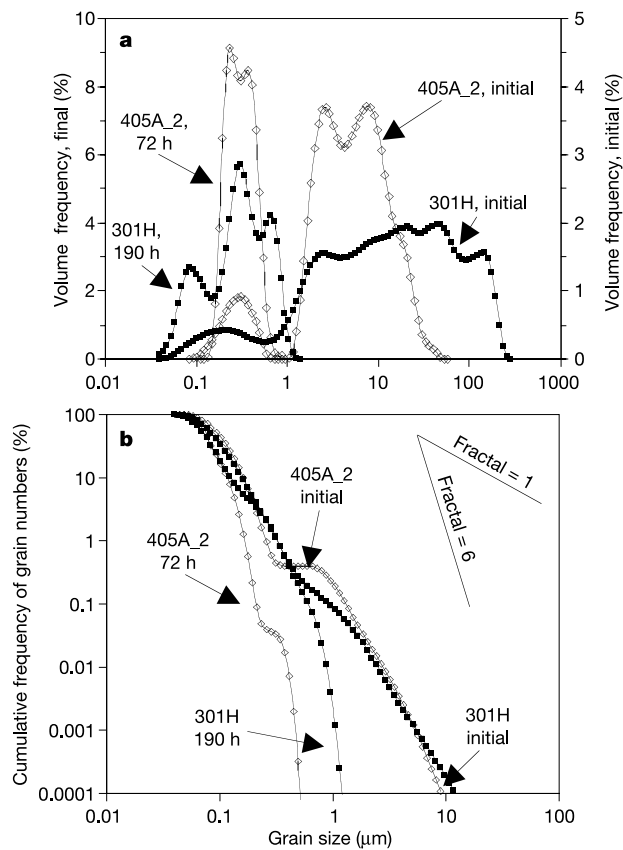


Figure 2 Particle size distribution (PSD) of two representative gouge samples measured for extended periods in a laser PSD analyser (see Methods). Samples: 301H, San Andreas fault (solid squares) and 405A_2, Bosman fault, South Africa (open diamonds). **a**, Grain size frequencies by volume. Each sample is displayed by two curves, one for the initial stage (right axis) and one for the final stage (left axis). A small fraction of the initial stage is smaller than 1 μm, whereas almost all grains of the final stage are smaller than 1 μm. **b**, Cumulative frequencies of grain numbers. A self-similar population should appear linear here, and fractal slopes of 1 and 6 (marked) seem to bound most of the curves.

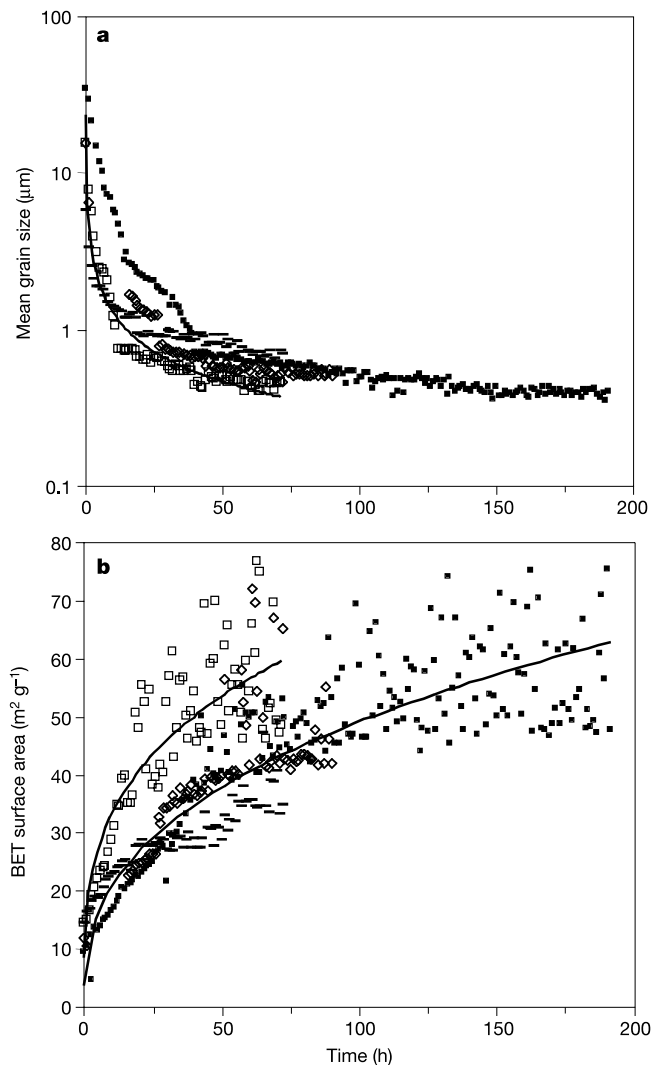


Figure 3 Time drift for four gouge samples measured for 72–190 h. **a**, Mean grain size; **b**, surface area. The plotted equivalent BET surface areas were calculated from the spherical grain area and the roughness parameter λ (text). Samples X-15 (open squares) and 301H (filled squares) are from the San Andreas fault; samples 405A_2 (open diamonds) and 405A_4 (filled oblongs) are from the Bosman fault, South Africa; four additional long-term runs with similar results are not plotted for clarity. Solid lines are power-law fits to representative samples.

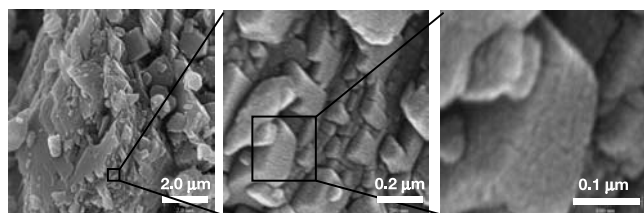


Figure 4 Scanning electron microscope images of untreated gouge from San Andreas fault, with an order-of-magnitude resolution increase from left to right. The gouge samples were mounted onto colloidal graphite coating covering upper portions of platinum trays, and sputter-coated with gold–palladium under vacuum. Note the particles of 0.02–0.05 μm in the middle and right frames.

event. In such a case, the observed gouge zone 70–100 m wide was formed by 7,000–10,000 earthquakes, which is in agreement with estimates of recurrence intervals. Although the present observations on gouge energetics are in accord with some studies³⁰, they contradict common thought that gouge surface energy is a negligible component of earthquake energy balance^{3,9}. If our conclusions are valid in general, they could explain, for example, the heat flow anomaly of the San Andreas fault system⁶. □

Methods

We employ a Beckman Coulter LS230 laser diffraction particle size analyser. Its 750-nm laser source and proprietary polarization intensity differential scattering (PIDS) technology provide detection limits of 0.04–2,000 μm . Spectrometry by laser diffraction does not discern between primary particles and agglomerates and is therefore sensitive to the degree of agglomeration inside the analyser^{14,17}. Disaggregation is a time-dependent process that can occur over the course of days in silicate mineral suspensions¹⁷. Accordingly, gouge PSD measurements lasting up to 190 h were taken, during which progressive disaggregation could be discerned (Figs 2, 3). Initial sonication accelerated disaggregation but had no noticeable influence on the final PSD. Ultrafine particles might reaggregate during the analysis¹⁴, as indicated by the increased scatter in surface area at long times (Fig. 3b). Power-law disaggregation (Fig. 3) and recurring agglomeration/disaggregation during analysis indicates that PSD and surface area results are conservative estimates of primary gouge particle size and area produced by the seismic slip. Ultrafine particles could also have been lost as a result of Ostwald ripening and volatilization during sampling and handling.

The collected gouge samples were sealed at the site and stored in plastic bags. For the PSD measurements, tens of micrograms of sample were added to 25 ml of an aqueous surfactant solution (usually 1% analytical reagent grade sodium metaphosphate prepared with doubly distilled water) or methanol and then subjected for 30 min to a low-energy sonic bath. After an additional 30 min this slurry was added to the laser analyser containing 125 ml of the same solution. Measurements of the diffraction spectrum were performed with continuous circulation inside the analyser, and PIDS was used in all reported runs. Spectral analysis was performed with proprietary software using the Mie scattering model¹⁴, with constants for the complex refractive index plus wavelength dependence for quartz¹⁴ and an absorption coefficient of 0.01.

Received 4 December 2004; accepted 28 January 2005; doi:10.1038/nature03433.

1. Sammis, C. G., Osborne, R. H., Anderson, J. L., Banerdt, M. & White, P. Self-similar cataclasis in the formation of fault gouge. *Pure Appl. Geophys.* **124**, 53–78 (1986).
2. Marone, C. & Scholz, C. Particle-size distribution and microstructures within simulated fault gouge. *J. Struct. Geol.* **11**, 799–814 (1989).
3. Scholz, C. H. *The Mechanics of Earthquakes and Faulting* (Cambridge Univ. Press, London, 2002).
4. Dor, O., Reches, Z. & van Aswegen, G. in *Rockburst and Seismicity in Mines* Vol. 5 (eds van Aswegen, G., Durrheim, R. J. & Ortlepp, W. D.) 109–112 (South African Inst. of Mining and Metallurgy, Johannesburg, 2001).
5. Chester, F. M., Evans, J. P. & Biegel, R. L. Internal structure and weakening mechanisms of the San Andreas Fault. *J. Geophys. Res. Solid Earth* **98**, 771–786 (1993).
6. Zoback, M. D., Hickman, S. & Ellsworth, W. San Andreas Fault observatory at depth. (<http://www.icdp.gfz Potsdam.de/html/sites/sanandreas/objectives/proposal.html>) (2002).
7. Ben-Zion, Y. & Sammis, C. G. Characterization of fault zones. *Pure Appl. Geophys.* **160**, 677–715 (2003).
8. Sleep, N. H. & Blanpied, M. L. Creep, compaction, and the weak rheology of major faults. *Nature* **359**, 687–692 (1992).
9. Olgaard, D. & Brace, W. The microstructure of gouge from a mining-induced seismic shear zone. *Int. J. Rock Mech. Mining Sci.* **20**, 11–19 (1983).
10. Steacy, S. J. & Sammis, C. G. An automaton for fractal patterns of fragmentation. *Nature* **353**, 250–252 (1991).
11. An, L. J. & Sammis, C. G. Particle-size distribution of cataclastic fault materials from southern California—a 3-d study. *Pure Appl. Geophys.* **143**, 203–227 (1994).
12. Kanamori, H. Mechanics of earthquakes. *Annu. Rev. Earth Planet. Sci.* **22**, 207–237 (1994).
13. Brune, J. N. Fault-normal dynamic unloading and loading: an explanation for 'nongouge' rock powder and lack of fault-parallel shear bands along the San Andreas Fault. *Eos* **8**, 47 (2001).
14. Xu, R. *Particle Characterization: Light Scattering Methods* (Kluwer Academic, Dordrecht, 2000).

15. Gregg, S. J. & Sing, K. S. W. *Adsorption, Surface Area and Porosity* (Academic, London, 1982).
16. Dewers, T. A., Wilson, B. & Reches, Z. Scaling particle size in fault gouge: Variable fractal dimension or non-fractal distribution? *Eos* **84**, NG12C-06 (2003).
17. Franco, F., Perez-Maqueada, L. A. & Perez-Rodriguez, J. L. The effect of ultrasound on the particle size and structural disorder of a well-ordered kaolinite. *J. Colloid Interface Sci.* **274**, 107–117 (2004).
18. Evans, J. P. & Chester, F. M. Fluid–rock interaction in faults of the San-Andreas System—Inferences from San-Gabriel fault rock geochemistry and microstructures. *J. Geophys. Res.* **100**, 13007–13020 (1995).
19. Wilson, B. *Meso- and Micro-structural Analysis of the San Andreas Fault at Tejon Pass, California*. Thesis, Univ. Oklahoma, Norman (2004).
20. Smith, B. & Dandwell, D. Coulomb stress accumulation along the San Andreas Fault system. *J. Geophys. Res.* **108**, 2296 (2003).
21. McGarr, A., Spottiswoode, S. M., Gay, N. C. & Ortlepp, W. D. Observations relevant to seismic driving stress, stress drop, and efficiency. *J. Geophys. Res.* **84**, 2251–2261 (1978).
22. Ogasawara, H., Yanagidani, Y. & Ando, M. (eds) *Seismogenic Process Monitoring* (Balkema, Rotterdam, 2002).
23. Ortlepp, W. D. *Rock Fracture and Rockbursts* (South Africa Institute of Mining and Metallurgy, Monograph series M9, 1997).
24. Hochella, M. F. Jr & Banfield, J. F. in *Chemical Weathering Rates of Silicate Minerals* (eds White, A. F. & Brantley, S. L.) 353–406 (Mineralogical Society of America, Washington DC, 1995).
25. Poliakov, A. N. B., Dmowska, R. & Rice, J. R. Dynamic shear rupture interactions with fault bends and off-axis secondary faulting. *J. Geophys. Res.* **107**, 2295 (2002).
26. Li, V. C. in *Fracture Mechanics of Rocks* (ed. Atkinson, B. K.) 351–428 (Academic, London, 1987).
27. Yund, R. A., Blanpied, M. L., Tullis, T. E. & Weeks, J. D. Amorphous material in high strain experimental fault gouges. *J. Geophys. Res.* **95**, 15589–15602 (1990).
28. Reches, Z. & Dewers, T. A. Gouge formation by dynamic pulverization during earthquakes. *Earth Planet. Sci. Lett.* (submitted).
29. Grady, D. E. & Kipp, D. E. Geometric statistics and dynamic fragmentation. *J. Appl. Phys.* **58**, 1210–1222 (1985).
30. Reches, Z. Mechanisms of slip nucleation during earthquakes. *Earth Planet. Sci. Lett.* **170**, 475–486 (1999).

Acknowledgements We thank the US National Science Foundation and the Southern California Earthquake Center for supporting this research.

Authors' contributions All authors contributed equally to this work.

Competing interests statement The authors declare that they have no competing financial interests.

Correspondence and requests for materials should be addressed to Z.R. (reches@ou.edu).

New material of the earliest hominid from the Upper Miocene of Chad

Michel Brunet¹, Franck Guy^{1,2}, David Pilbeam², Daniel E. Lieberman², Andossa Likius³, Hassane T. Mackaye³, Marcia S. Ponce de León⁴, Christoph P. E. Zollikofer⁴ & Patrick Vignaud¹

¹Laboratoire de Géobiologie, Biochronologie et Paléontologie Humaine, CNRS UMR 6046, Faculté des Sciences, Université de Poitiers, 40 Avenue du Recteur Pineau, 86022 Poitiers Cedex, France

²Peabody Museum, Harvard University, 11 Divinity Avenue, Cambridge, Massachusetts 02138, USA

³Université de N'Djamena, BP 1117, N'Djamena, Tchad

⁴Anthropologisches Institut/MultiMedia Laboratorium, Universität Zürich-Irchel, Winterthurerstrasse 190, 8057 Zürich, Switzerland

Discoveries in Chad by the Mission Paléanthropologique Franco-Tchadienne have substantially changed our understanding of early human evolution in Africa^{1–3}. In particular, the TM 266 locality in the Toros-Menalla fossiliferous area yielded a nearly complete cranium (TM 266-01-60-1), a mandible, and several isolated teeth assigned to *Sahelanthropus tchadensis*³ and biochronologically dated to the late Miocene epoch (about 7 million years ago). Despite the relative completeness of the TM 266 cranium, there has been some controversy about its morphology and its status in the hominid clade^{4,5}. Here we describe new dental and mandibular specimens from three Toros-Menalla (Chad) fossiliferous localities (TM 247, TM 266 and TM 292) of